Three-dimensional force microscopy of cells in biopolymer networks

Julian Steinwachs[1], Claus Metzner[1], Kai Skodzek[1], Nadine Lang[1], Ingo Thievessen[1], Christoph Mark[1], Stefan Münster[2], Katerina E Aifantis[3] & Ben Fabry[1]

We describe a technique for the quantitative measurement of cell-generated forces in highly nonlinear three-dimensional biopolymer networks that mimic the physiological situation of living cells. We computed forces of MDA-MB-231 breast carcinoma cells from the measured network deformations around the cells using a finite-element approach based on a constitutive equation that captures the complex mechanical properties of diverse biopolymers such as collagen gels, fibrin gels and Matrigel. Our measurements show that breast carcinoma cells cultured in collagen gels generated nearly constant forces regardless of the collagen concentration and matrix stiffness. Furthermore, time-lapse force measurements showed that these cells migrated in a gliding motion with alternating phases of high and low contractility, elongation, migratory speed and persistence.

The migration of cells through the fibrous network of the extra-cellular matrix is an integral part of many biological processes, including tissue morphogenesis, wound healing and cancer metastasis[1]. To migrate through the pores of the dense meshwork of the extracellular matrix, cells must generate considerable forces that are exerted on the matrix[2–5]. Accurate measurement of these traction forces is crucial for understanding the invasion of cancer cells or the migration of immune cells in tissue[5,6].

One can estimate traction forces by culturing cells on artificial two-dimensional (2D) or three-dimensional (3D) substrates with known stiffness and measuring the substrate deformations as the cells adhere and migrate[7–11]. Present methods for traction-force reconstruction rely on the linear force-displacement response of the substrate. However, the connective tissues of most organs are highly nonlinear, as are reconstituted tissue equivalents such as collagen and fibrin gels, both of which stiffen strongly under shear[12–14] and collapse with an abnormal apparent Poisson's ratio greater than 1 when stretched[15–18] (**Fig. 1**).

In this report we describe a method for measuring cell traction forces in physiologically relevant 3D biopolymer networks with highly nonlinear mechanical properties. With our method, we studied the contractility, migration and shape changes of breast carcinoma cells in collagen gels with differing concentrations and matrix stiffness. During migration, breast carcinoma cells underwent alternating phases of high and low contractility, elongation, migratory speed and persistence, all of which showed high temporal correlation. On average, these cells did not respond to higher matrix stiffness with greater contractility, which can be partially explained by impaired cell elongation in denser gels.

RESULTS

Macrorheology and constitutive equation for collagen gels

To measure 3D cell traction from the deformation of the surrounding collagen network matrix, we combined existing micromechanical models with a continuum description: on a small spatial scale corresponding to a fiber segment, we considered that the local deformation of the fiber segment does not follow the deformation of the bulk. This so-called non-affine behavior is caused by fiber buckling, straightening or stretching[14,19–24] and gives rise to a pronounced nonlinear stress-strain relationship and collapse of the material under uniaxial stretch (**Fig. 1a,b**). Beyond the length scale of the typical interconnection distance, however, the strain of the fiber approximates the macroscopic strain λ (ref. 14), depending on the orientation of the fiber and the applied deformation (equation (2)). We assumed that deformations become affine for a sufficiently large volume of material, and thus we were able to compute the stress-strain response by averaging the force contributions of all fibers contained in such a volume[12] (**Fig. 1c**).

The mechanical properties of collagen fibers can be described by a nonlinear potential function $w(\lambda)$ with stiffness $w''(\lambda)$ that exhibits three distinct regimes (equation (1)). Under compression, the fibers buckle, and the stiffness falls exponentially with a characteristic strain scale d_0. For small extensions, the fibers have a constant stiffness κ_0. If the fibers are stretched beyond the linear strain range λ_s, the stiffness increases exponentially with a characteristic strain scale d_s (**Fig. 1e**). By averaging the stress contributions of many fibers[12], assuming an isotropic and homogeneous distribution (**Supplementary Notes 1–3**), one can derive a constitutive equation (equation (3)) that describes the mechanical behavior of the bulk material.

Figure 1 | Macrorheology of collagen type I gels and semi-affine model description. (**a**) Shear stress versus shear strain of a 2.4–mg ml^{-1} collagen gel measured in a cone-plate rheometer (representative of $n = 5$). Lin. mat., predictions from a linear material model; Col. const. eq., predictions from a constitutive equation for collagen gels. (**b**) Vertical contraction and expansion of a 2.4–mg ml^{-1} collagen gel under uniaxial compression and stretch. Lines color-coded according to the key in **a**. (**c**) Non-affine deformations (stretch and compression) of individual collagen fibers, depending on their orientation. (**d**) Fiber buckling under compressional strain ($\lambda < 0$), fiber straightening under small extensional strain ($0 < \lambda < \lambda_s$) and fiber stretching under large extensional strain ($\lambda_s < \lambda$). (**e**) Fiber stiffness versus fiber strain ($w''(\lambda)$) for the same regimes shown in **d**, characterized by an exponential decrease with a characteristic strain scale d_0 for buckling, a constant stiffness κ_0 for small extensional strain and an exponential increase with a characteristic strain scale d_s for large extensional strain.
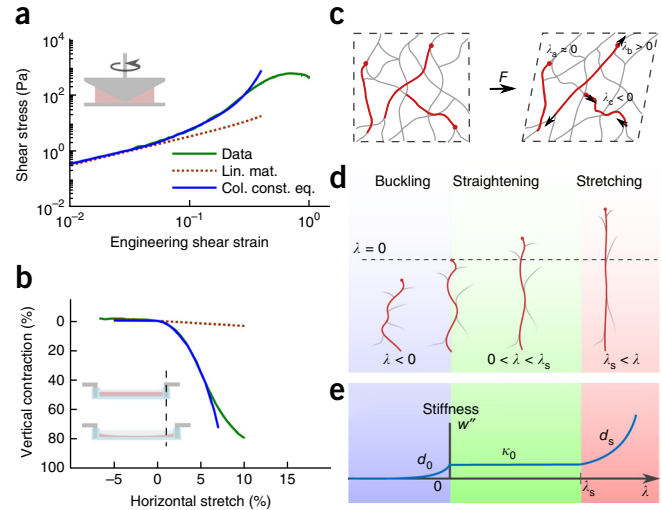
We determined the four parameters of our constitutive equation (d_0, κ_0, λ_s and d_s) by means of two types of experiments. First, we measured the stress-strain relationship for simple shear deformation in a cone-plate rheometer (**Fig. 1a**). We found a linear regime followed by pronounced strain stiffening beyond a shear of ~3% that was well described by an exponential behavior[13,16,21]. Second, we measured the vertical (z) contraction of collagen gel when it was uniaxially stretched in the x-direction while the strain in the y-direction was fixed at 0% (**Fig. 1b**). Collagen gels exhibited strong vertical contraction under stretch, with a horizontal-to-vertical stretch ratio of ~8 (**Fig. 1b**), indicating an apparent Poisson's ratio considerably greater than 1. Additionally, we measured the horizontal gel dilation under uniaxial compression. The gel expanded only weakly in the vertical direction, revealing the fundamental asymmetry of the material resulting from fiber buckling (**Fig. 1b**).

Our material model (equation (3)) reproduced our experimental data (the strain stiffening, the high apparent Poisson's ratio and the stretch-versus-compression asymmetry) well up to 30% of compression, 30% of shear and 7% of uniaxial stretch (**Fig. 1**). Moreover, measurements of collagen gels with different concentrations (0.6, 1.2 and 2.4 mg ml^{-1}), fibrin gels and Matrigel showed that our material model captured the rheology of these biopolymer networks (**Supplementary Notes 4–8**).

This constitutive equation allowed us to compute the gel deformations and stress in response to arbitrary forces, geometries and boundary conditions using a finite-element approach. For finite-element analysis, we represented the geometry of the gel with a mechanically coupled mesh of simple tetrahedra (**Supplementary Note 2**). Our analysis showed that collagen gels stiffened strongly under dilating forces of cells, resulting in steric hindrance against migration (**Supplementary Note 9**). In contrast, gel stiffening was weak with contracting cell forces. This mechanical behavior of collagen gels led to more efficient migration for elongated cells with polarized tractions (**Supplementary Note 9**).

Experimental validation with point-like forces

To experimentally test the validity of the material model in combination with the finite-element approach, we applied forces of 10–30 nN using 5-μm magnetic beads attached to the surface of a collagen gel in a magnetic-tweezers setup (**Fig. 2a,b**). We measured the resulting local gel displacement by tracking fluorescent marker beads in the gel (**Fig. 2c**). Time-lapse recordings

of the matrix response showed predominantly elastic behavior with negligible viscosity and plasticity (**Fig. 2** and **Supplementary Note 10**). We then predicted the local gel displacement from the known magnetic forces and the mechanical parameters of the gel as measured with an extensional rheometer (**Fig. 2f–h** and **Supplementary Note 5**). The predicted displacement field overestimated the maximum displacement near the bead but was in good agreement with measurements at distances of more than 50 μm from the point of force application (**Fig. 2g**). In particular, our measurements confirmed the model prediction of a highly asymmetric displacement field. We found that the gel deformed strongly under tension (**Fig. 2**) but not under compression, as compressive stresses propagated poorly owing to fiber buckling. By contrast, the displacement field in a linear material (**Fig. 2h**) was centered on the external force.

In a second test, we reconstructed the applied point-like force of the magnetic bead from the measured collagen displacement field. We minimized the mismatch between the simulated and the measured local gel displacement by adjusting the position, direction and magnitude of the simulated force. The fitted force position, on average, coincided precisely with the centroid of the measured bead position, with an s.d. of 4 μm for different measurements (**Fig. 2d**). The fitted force amplitude was on average 22% higher than the applied magnetic force, with an s.d. of 33% for different measurements (**Fig. 2e**).

Unconstrained 3D force reconstruction

In contrast to the point-like force on a magnetic bead, the spatial distribution of forces around living cells is unknown. Unconstrained force reconstruction does not rely on cell-surface information and makes no prior assumptions about the 3D force field of the cell. This creates a computational problem, as the number of fit parameters (force vectors) is the same as the number of measured data points (displacement vectors). To prevent overfitting, we introduced a regularization approach that allowed cell forces to be present only in a portion of the measured volume. Each node of the finite-element mesh was assigned a weight with which external forces at that node were penalized. When the penalty was iteratively lowered for nodes with high forces, the prevailing cell forces condensed onto a few nodes, and small forces due to uncorrelated measurement noise were minimized

Figure 2 | Experimental validation of the constitutive equation for collagen gels. (**a**) Image recordings (representative of 13 measurements) of the magnetic bead, small fiducial marker beads and the magnetic needle tip during force application at different time points (in green) overlaid with an image of the unstrained configuration (in magenta). Colors from fiducial markers that did not move grade to black. Scale bar, 20 μm. (**b**) Brightfield image of the magnetic-tweezers experiment. The dashed circle corresponds to the dashed circle in **d**. (**c**) Overlay of fluorescent images of the marker beads before (cyan) and after (red) a force of 20 nN was applied to the beads. Red arrow indicates the direction of the applied force as in **b**. (**d**) Reconstructed forces (position, direction and magnitude) of magnetic beads from 13 independent measurements. The length of the lines is normalized to the magnitude of the known applied force (red). The dashed circle corresponds to the dashed circle in **b**. (**e**) Reconstructed force magnitude versus applied force magnitude. Horizontal error bars indicate the error (r.m.s.) in the applied force due to variations in bead size. (**f**) Simulated displacement around a point-like force of 20 nN. Col. gel., collagen gel. (**g**) Measured displacement around a point-like force of 20 nN averaged (avg.) over 13 measurements. Inset shows the local matrix displacements (Displ.) along the x-axis through the point of force application (at x = 0). Simulated displacements are shown in blue, individual measurements from different beads are in gray, and the average is in red. Pos., position. (**h**) Simulated displacements around a point-like force of 20 nN for a linear material (lin. mat.).
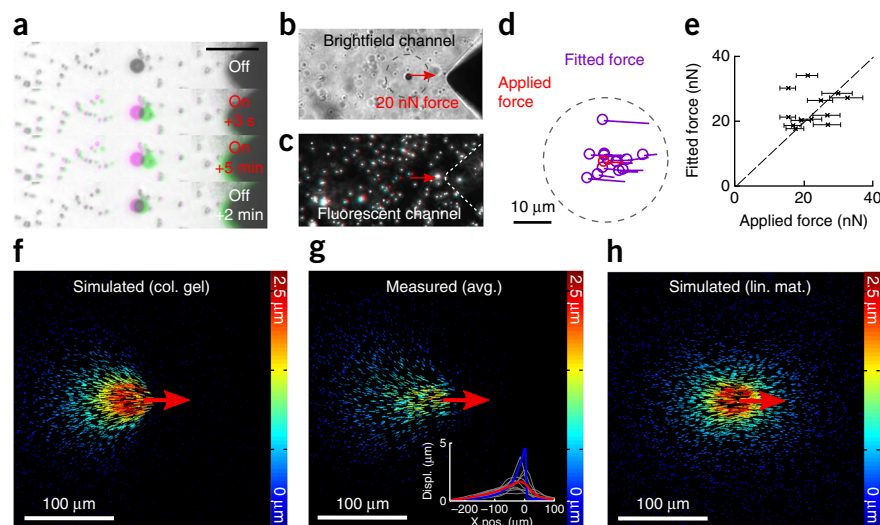
in the rest of the volume. The strength of the regularization was controlled by the parameter α. By running unconstrained force reconstruction on the above-described data set of matrix displacements around a point-like force, we found that the total force (the vector sum of all forces around the magnetic bead) depended little on α for values less than 0.3 pN^2 μm^{-2} (**Supplementary Note 11**). The systematic force error was less than 1% with an s.d. of 30% between individual measurements. When averaged over many beads, however, the reconstructed forces appeared blurred and were systematically shifted 30 μm away from the direction of force application (Discussion).

Traction forces of living cells
To measure the force-induced deformation of a collagen gel, we imaged the collagen network around the cells with confocal

reflection microscopy before and after force relaxation with cytochalasin D and evaluated the local displacement field via 3D particle image velocimetry (**Fig. 3** and **Supplementary Note 12**). Unconstrained reconstructed cellular forces were localized near but not exactly on the surfaces of cells (**Fig. 3b,c**). To quantify this error, we projected the cellular force together with brightfield images of a given cell onto the x-y plane and plotted the average force density versus the distance to the cell edge. Forces were systematically shifted away from the cell edge by approximately 18 μm (**Fig. 3f**) (see Discussion).

In addition to cell forces, our model allowed us to compute the principal matrix stress (**Fig. 3d**) and the principal matrix stiffness (**Fig. 3e**). Both tended toward zero in the region of the cell where the material was compressed and the fibers buckled, in essence creating a hole where the contracting cell was located. This suggests that cell forces are used almost exclusively to pull collagen fibers centripetally toward the cell. Therefore, our approach describing cellular forces as a 3D force field in a
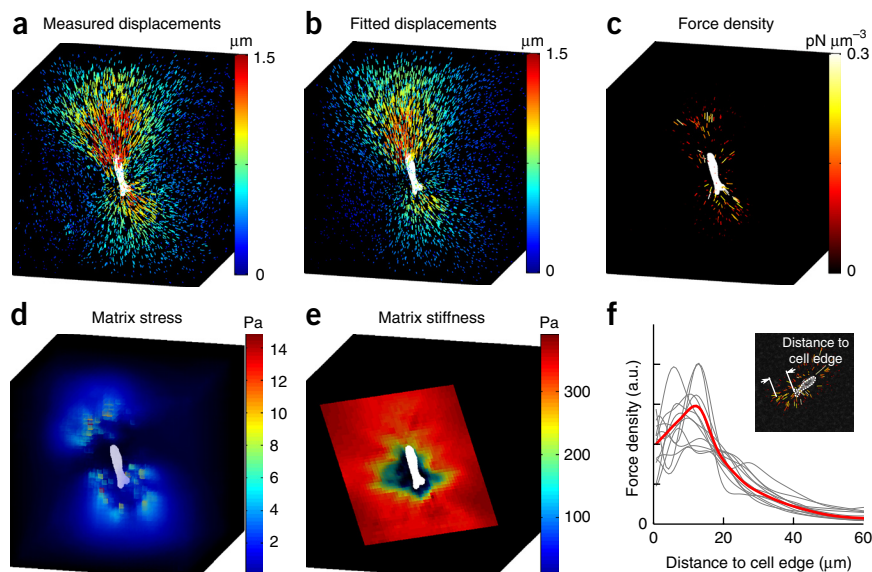

Figure 3 | Reconstruction of cellular forces inside a 1.2–mg ml^{-1} collagen gel. (**a**) Measured displacements around a single MDA-MB-231 breast carcinoma cell. (**b**) Regularized displacement field around the cell in **a**. (**c**) Force density around the cell in **a** and **b** as calculated from the regularized displacements shown in **b**. (**d**) Principal matrix stress as calculated from the regularized displacement field. (**e**) Principal matrix stiffness as calculated from the regularized displacement field. (**f**) Reconstructed force density in arbitrary units (a.u.) around individual cells (n = 12; gray curves) as a function of the distance to the cell edge as illustrated in the inset. The average force density is shown in red.

Figure 4 | Contractility of MDA-MB-231 cells in gels with different collagen concentrations. (**a**) Collagen fiber network imaged using confocal reflection microscopy. (**b**,**c**) Linear Young's modulus of collagen gels (**b**) and pore diameter of the network (**c**). (**d**) Morphology of cells (actin in red, chromatin in green) embedded in collagen gel. (**e**,**f**) Cell elongation (**e**) and elongation of the nucleus (**f**) in cells embedded in collagen gel. (**g**) 3D matrix displacement fields of the collagen gel around embedded cells. Density and hue of marks indicate the magnitude of the local displacement vector. (**h**) Maximum cell-induced matrix displacement (Max. displ.). (**i**) Projected area of cells embedded in collagen gel. (**j**) 3D force density of cells embedded in collagen gels. Density and color intensity of marks are proportional to the local force density. Scale bars in **g**,**j**, 50 µm. (**k**,**l**) Total contractility (**k**) and force polarity (**l**) of cells in collagen gel. For all box plots, the central (red) mark indicates the median, the edges of the box denote the 25th and 75th percentiles, the whiskers extend to the most extreme data points not considered outliers, and outliers are plotted individually (red crosses). Notches indicate s.e. *$P \leq 0.05$, Student's t-test assuming unequal variances including the outliers. Col. con., collagen concentration; n.s., not significant ($P > 0.05$).
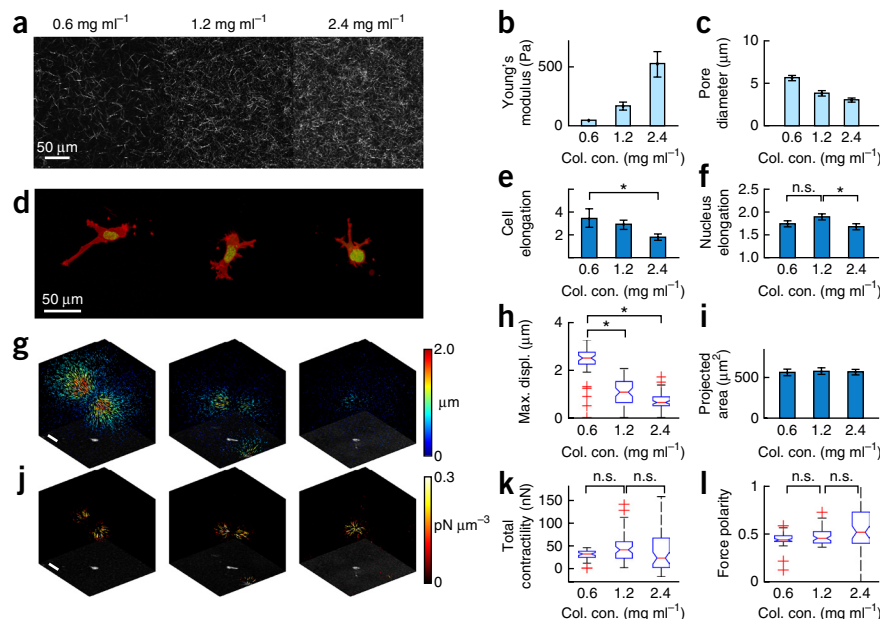
continuous material, without a 'hole' to accommodate the cell, does not lead to force overestimation[11].

As a measure of cell contractility, we quantified the total magnitude of the projected force vectors pointing toward the cell center (**Supplementary Note 13**). From a data set of 63 MDA-MB-231 cells in a 1.2–mg ml^{−1} collagen gel, we measured a total contractility of 47.6 ± 3.4 nN (geometric mean ± s.e.m.). The total contractility for the same cell line grown on a planar collagen-coated polyacrylamide substrate (Young's modulus: 5 kPa) has been reported[25,26] as ~270 nN.

To quantify the geometry of the 3D cellular force fields, we decomposed the contractile force into force contributions from three principal components of an orthogonal coordinate system aligned with the force field of the cell (**Supplementary Note 13**). For a force dipole, the force polarity approaches 1, whereas for an isotropic force field, the force polarity approaches 1/3. The force polarity of MDA-MB-231 cells was 0.47 ± 0.01 (mean ± s.e.m., $n = 63$), indicating that about half of the total contractility could be expressed by a single force dipole.

Contractile cell forces contribute to the strain stiffening of a collagen matrix surrounding cells. To quantify this, we computed for every cell the mechanical work needed to achieve a small additional matrix deformation. MDA-MB-231 cells stiffened the bulk of the collagen gel on average by 3.2% ± 0.5% (mean ± s.e.m.), in agreement with numerical simulations that also indicated little strain stiffening of the bulk of the collagen matrix around contractile cells (**Supplementary Note 9**). In contrast, the collagen matrix showed a pronounced stiffening response to dilatational forces that occur when a cell is attempting to squeeze through a narrow pore (**Supplementary Note 9**).

Constrained 3D force reconstruction
Unconstrained force reconstruction can robustly resolve total cell contractility down to 5 nN for displacement noise levels in excess of 200 nm, but the method has limited localization accuracy (**Fig. 3f**

and **Supplementary Notes 14–17**). To avoid the systematic shift and blurring of the reconstructed forces, one can constrain their localization to the cell surface. To demonstrate this, we fluorescently stained the cytoplasm of HT1080 fibrosarcoma cells, imaged the cells with confocal microscopy, and segmented them by thresholding. We assigned a zero-penalty weight to nodes of finite elements with a distance to the cell surface of less than half the mesh size; the remaining computation was identical to the unconstrained method. The force localization of the constrained method was superior to that of the unconstrained method (**Supplementary Note 18**), but both methods gave similar values for the total contractility and force polarity.

Traction forces in gels of varying collagen concentration
To study how cells respond to changes in matrix stiffness and density, we measured traction forces of MDA-MB-231 cells embedded in collagen gels with different concentrations (0.6 ($n = 48$), 1.2 ($n = 63$) and 2.4 mg ml^{−1} ($n = 64$)) where the linear stiffness increased from 44 Pa to 513 Pa and the average pore diameter decreased from 5.6 µm to 3.0 µm (**Fig. 4a–c**)[27]. Fluorescent staining of the actin cytoskeleton showed that cells in the denser gels were more rounded and had smaller and thinner protrusions than cells in gels with lower collagen concentrations (**Fig. 4d–f**). However, the projected cell area in these different gels, and therefore the cell volume, was the same. Matrix deformations induced by the cells decreased with increasing collagen concentration (**Fig. 4g–i**), but the total cell contractility, measured using unconstrained force reconstruction, remained the same, as did the force polarity (**Fig. 4j–l** and **Supplementary Note 19**).

Time-lapse force microscopy
Reflection microscopy minimizes photodamage and allows for long-term measurements (>24 h) of migration trajectories, cell morphology and traction forces (**Supplementary Videos 1** and **2**). To investigate the coordination of traction forces during cell migration
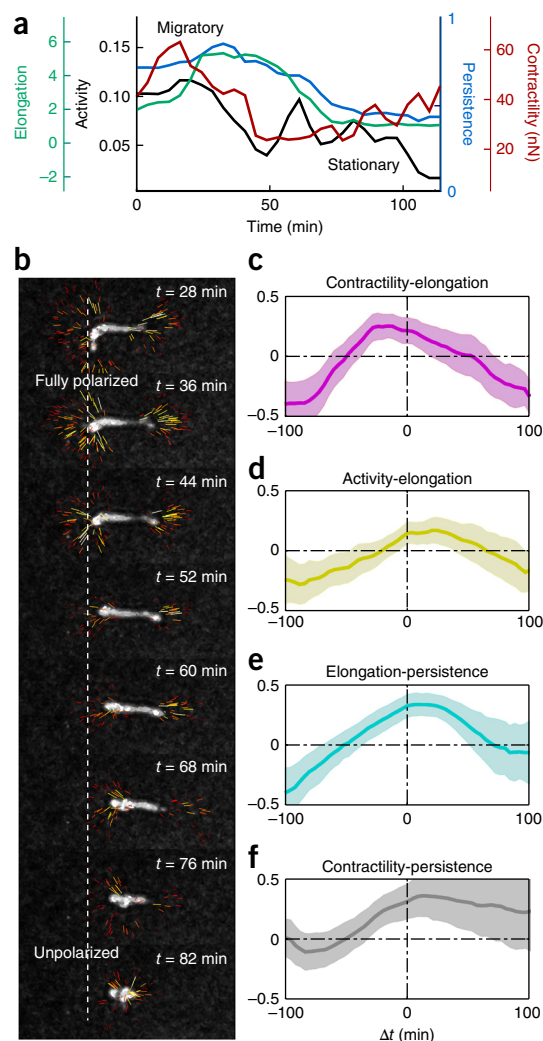
Figure 5 | Time-lapse force microscopy of a breast carcinoma cell inside collagen gel. (**a**) Time course of contractility, elongation, migratory activity and migratory persistence of an MDA-MB-231 breast carcinoma cell embedded in a 3D collagen gel (1.2 mg ml^{-1}). (**b**) Force field of the cell shown in **a**. (**c**–**f**) Cross-correlation of force fluctuations, cell morphology and migration parameters for different time lags averaged over 20 cells. (**c**) Contractility versus elongation. (**d**) Activity versus elongation. (**e**) Elongation versus persistence. (**f**) Contractility versus persistence. Shaded area around curves indicates ±1 s.e.

DISCUSSION

Our underlying assumption of the biopolymer network as a mechanical continuum is violated at the scale of individual fibers or single network pores. Therefore, the spatial resolution of the reconstructed forces is limited by the length scale at which the continuum assumption breaks down. Accordingly, we attribute the variability and positional errors in reconstructed forces in the magnetic bead experiments (**Fig. 2g**) to local heterogeneity in the fiber structure of the gels (density, fiber orientation, fiber thickness and connectivity) as described previously[29]. The spatial resolution of the reconstructed force is therefore limited to around 30 μm (**Supplementary Note 11**). Further, blurring of the reconstructed forces is caused by the size of the finite elements, the presence of measurement noise and the necessary regularization (**Supplementary Note 14**). Finally, collagen fibers under compression can bear only little mechanical stress, and therefore all discrepancies between the continuum model and the real situation of an inhomogeneous collagen gel must be reconciled by forces that arise in the tensed region of the collagen gel. If confocal image stacks of fluorescently labeled cells are available, one can avoid this problem by restricting the reconstructed forces to the cell surface (**Supplementary Note 18**).

Our statistical force fluctuations of 30% due to measurement errors are considerably smaller than the >50% fluctuations in the total force magnitude between individual cells (**Fig. 4k**). Therefore, our measurement error does not markedly degrade the quality of the data or require the measurement of a considerably larger number of cells for statistical significance. **Table 1** summarizes the sensitivity, accuracy and spatial resolution of the constrained and unconstrained 3D force reconstruction methods.

Our finding of constant traction forces for collagen gels of different densities and stiffness is in contrast to cell behavior on planar substrates, where cell tractions increase with higher substrate stiffness and with increasing ligand density[30–32]. A possible explanation that reconciles these conflicting findings is that a smaller pore size in the denser and stiffer 3D matrices may impede cell elongation and the formation of cell protrusions, and hence may reduce force generation. In support of this hypothesis, we found that the contractility of a subpopulation of elongated cells with an aspect ratio greater than 2.0 was significantly ($P < 0.05$, Student's two-tailed t-test assuming unequal variances) greater in 1.2 mg ml^{-1} collagen gels than in 0.6 mg ml^{-1} collagen gels (**Supplementary Note 21**).

Our method can be used to study the dynamics of cell migration in a 3D environment. We noted that untreated MDA-MB-231 cells alternated between highly migratory and more stationary phases. During migratory phases cells had an elongated shape and high contractility. The cross-correlation between these parameters was highest for a time lag of zero. Thus we found no evidence that phases of elongation, contraction and motility

through a disordered 3D collagen matrix, we simultaneously measured the time course of contractility, cell elongation, migration persistence p and migration activity a (calculated from the momentary cell speed v according to $a = v(1 - p^2)^{0.5}$ (**Fig. 5a,b**)[28]. We found that for MDA-MB-231 cells, all four parameters were significantly correlated for time lags between 0 and ±15 min (**Fig. 5c**–**f** and **Supplementary Note 20**). This implies that phases of rapid cell movements with high persistence and activity were accompanied by large contractile forces and pronounced cell elongation. Conversely, phases during which the cells remained stationary were accompanied by small contractile forces and more rounded cell shapes. For lag times greater than ±1 h, the correlations between these parameters were negative, implying that migratory phases lasted for approximately 1 h. Moreover, phases of high contractility were accompanied by further cell lengthening (**Supplementary Note 20**).

Table 1 | Sensitivity, accuracy (error) and spatial resolution of 3D force reconstruction

	Unconstrained	Constrained
Sensitivity	5 nN[a]	5 nN[a]
Error (relative bias ± s.d.)	<1% ± 30%[b]	+22% ± 33%[b]
Spatial resolution (bias ± s.d.)	30 μm ± 30 μm[b,c]	0 μm ± 4 μm[b]

[a]For a 384-Pa (Young's modulus) collagen gel and 60-nm spatial resolution of local gel displacement. [b]For a point force of 10–30 nN. [c]Spatial bias is in the force direction.

are shifted relative to one another, as one would expect with an 'inchworm' type of motion in which contraction leads to cell shortening and force relaxation leads to cell lengthening. Rather, during the migratory phases, MDA-MB-231 cells seemed to glide through the gel in a steady process of simultaneous adhesion and de-adhesion.

These results demonstrate that our 3D traction force microscopy method can contribute to understanding of the physical mechanisms of cell migration in physiologically relevant environments.

METHODS
Methods and any associated references are available in the online version of the paper.

Note: Any Supplementary Information and Source Data files are available in the online version of the paper.

COMPETING FINANCIAL INTERESTS
The authors declare no competing financial interests.

Reprints and permissions information is available online at http://www.nature.com/reprints/index.html.

1. Friedl, P., Zanker, K.S. & Brocker, E.B. Cell migration strategies in 3-D extracellular matrix: differences in morphology, cell matrix interactions, and integrin function. *Microsc. Res. Tech.* **43**, 369–378 (1998).
2. Zaman, M.H. *et al.* Migration of tumor cells in 3D matrices is governed by matrix stiffness along with cell-matrix adhesion and proteolysis. *Proc. Natl. Acad. Sci. USA* **103**, 10889–10894 (2006).
3. Friedl, P. & Wolf, K. Proteolytic interstitial cell migration: a five-step process. *Cancer Metastasis Rev.* **28**, 129–135 (2009).
4. Friedl, P., Wolf, K. & Lammerding, J. Nuclear mechanics during cell migration. *Curr. Opin. Cell Biol.* **23**, 55–64 (2011).
5. Koch, T.M., Muenster, S., Bonakdar, N., Buttler, J.P. & Fabry, B. 3D traction forces in cancer cell invasion. *PLoS ONE* **7**, e33476 (2012).
6. Lämmermann, T. *et al.* Rapid leukocyte migration by integrin-independent flowing and squeezing. *Nature* **453**, 51–55 (2008).
7. Dembo, M. & Wang, Y.L. Stresses at the cell-to-substrate interface during locomotion of fibroblasts. *Biophys. J.* **76**, 2307–2316 (1999).
8. Butler, J.P., Tolic-Norrelykke, I.M., Fabry, B. & Fredberg, J.J. Traction fields, moments, and strain energy that cells exert on their surroundings. *Am. J. Physiol. Cell Physiol.* **282**, C595–C605 (2002).
9. Sabass, B., Gardel, M.L., Waterman, C.M. & Schwarz, U.S. High resolution traction force microscopy based on experimental and computational advances. *Biophys. J.* **94**, 207–220 (2008).
10. Legant, W.R. *et al.* Multidimensional traction force microscopy reveals out-of-plane rotational moments about focal adhesions. *Proc. Natl. Acad. Sci. USA* **110**, 881–886 (2013).
11. Legant, W.R. *et al.* Measurement of mechanical tractions exerted by cells in three-dimensional matrices. *Nat. Methods* **7**, 969–971 (2010).
12. Storm, C., Pastore, J.J., MacKintosh, F.C., Lubensky, T.C. & Janmey, P.A. Nonlinear elasticity in biological gels. *Nature* **435**, 191–194 (2005).
13. Arevalo, R.C., Urbach, J.S. & Blair, D.L. Size-dependent rheology of type-I collagen networks. *Biophys. J.* **99**, L65–L67 (2010).
14. Münster, S. *et al.* Strain history dependence of the nonlinear stress response of fibrin and collagen networks. *Proc. Natl. Acad. Sci. USA* **110**, 12197–12202 (2013).
15. Voytik-Harbin, S.L., Roeder, B.A., Sturgis, J.E., Kokini, K. & Robinson, J.P. Simultaneous mechanical loading and confocal reflection microscopy for three-dimensional microbiomechanical analysis of biomaterials and tissue constructs. *Microsc. Microanal.* **9**, 74–85 (2003).
16. Vader, D., Kabla, A., Weitz, D. & Mahadevan, L. Strain-induced alignment in collagen gels. *PLoS ONE* **4**, e5902 (2009).
17. Roeder, B.A., Kokini, K. & Voytik-Harbin, S.L. Fibril microstructure affects strain transmission within collagen extracellular matrices. *J. Biomech. Eng.* **131**, 031004 (2009).
18. Brown, A.E., Litvinov, R.I., Discher, D.E., Purohit, P.K. & Weisel, J.W. Multiscale mechanics of fibrin polymer: gel stretching with protein unfolding and loss of water. *Science* **325**, 741–744 (2009).
19. Onck, P.R., Koeman, T., van Dillen, T. & van der Giessen, E. Alternative explanation of stiffening in cross-linked semiflexible networks. *Phys. Rev. Lett.* **95**, 178102 (2005).
20. Heussinger, C., Schaefer, B. & Frey, E. Nonaffine rubber elasticity for stiff polymer networks. *Phys. Rev. E* **76**, 031906 (2007).
21. Stein, A.M., Vader, D.A., Weitz, D.A. & Sander, L.M. The micromechanics of three-dimensional collagen-I gels. *Complexity* **16**, 22–28 (2011).
22. Sheinman, M., Broedersz, C.P. & MacKintosh, F.C. Nonlinear effective-medium theory of disordered spring networks. *Phys. Rev. E* **85**, 021801 (2012).
23. Stylianopoulos, T. & Barocas, V.H. Volume-averaging theory for the study of the mechanics of collagen networks. *Comput. Methods Appl. Mech. Eng.* **196**, 2981–2990 (2007).
24. Licup, A.J. *et al.* Stress controls the mechanics of collagen networks. *Proc. Natl. Acad. Sci. USA* **112**, 9573–9578 (2015).
25. Kraning-Rush, C.M., Carey, S.P., Califano, J.P., Smith, B.N. & Reinhart-King, C.A. The role of the cytoskeleton in cellular force generation in 2D and 3D environments. *Phys. Biol.* **8**, 015009 (2011).
26. Lautscham, L.A. *et al.* Migration in confined 3D environments is determined by a combination of adhesiveness, nuclear volume, contractility, and cell stiffness. *Biophys. J.* **109**, 900–913 (2015).
27. Lang, N.R. *et al.* Estimating the 3D pore size distribution of biopolymer networks from directionally biased data. *Biophys. J.* **105**, 1967–1975 (2013).
28. Metzner, C. *et al.* Superstatistical analysis and modelling of heterogeneous random walks. *Nat. Commun.* **6**, 7516 (2015).
29. Mickel, W. *et al.* Robust pore size analysis of filamentous networks from 3D confocal microscopy. *Biophys. J.* **95**, 6072–6080 (2008).
30. Pelham, R.J. Jr. & Wang, Y. Cell locomotion and focal adhesions are regulated by substrate flexibility. *Proc. Natl. Acad. Sci. USA* **94**, 13661–13665 (1997).
31. Engler, A. *et al.* Substrate compliance versus ligand density in cell on gel responses. *Biophys. J.* **86**, 617–628 (2004).
32. Reinhart-King, C.A., Dembo, M. & Hammer, D.A. The dynamics and mechanics of endothelial cell spreading. *Biophys. J.* **89**, 676–689 (2005).

ONLINE METHODS

Biopolymer gel synthesis. We mixed rat tail collagen (Collagen R, 2 mg/ml, Matrix Bioscience, Berlin, Germany) and bovine skin collagen (Collagen G, 4 mg/ml, Matrix Bioscience) at a ratio of 1:1. We then added 10% (vol/vol) sodium bicarbonate (23 mg/ml) and 10% (vol/vol) 10× DMEM (Gibco). We adjusted the solution to pH 10 with 43 µl of 1 M NaOH and polymerized it at 37 °C, 95% humidity and 5% CO_2 for 1 h. For final collagen concentrations of 1.2 mg/ml and 0.6 mg/ml, we diluted the solution before polymerization with a mixture of 1 volume part $NaHCO_3$, 1 part 10× DMEM and 8 parts H_2O. We polymerized fibrin gels with a final concentration of 4.0 mg/ml human fibrinogen after mixing with 0.05 NIH units/ml human α-thrombin (both from Haemochrome Diagnostics) in buffer containing 0.15 M NaCl, 20 mM CaCl, 25 mM HEPES at pH 7.4 for 1 h at room temperature. We polymerized Matrigel (BD Bioscience) at a concentration of 10 mg/ml (undiluted) at 37 °C, 5% CO_2 and 95% relative humidity for 1 h.

Mechanical description of collagen gels. We assumed that the collagen network deforms in an affine way beyond a certain length scale, and that below that scale, individual fiber segments deform in a non-affine way and evade mechanical stress using their internal degrees of freedom (**Fig. 1d**). This can be described by a nonlinear and asymmetric energy potential function $w(\lambda)$ = $w(\Delta l/l)$ of the fibers. The potential function $w(\lambda)$ of individual collagen fibers is expected to exhibit three distinct regimes: buckling, straightening and stretching. The differential fiber stiffness $w''(\lambda)$ can thus be described with only four parameters: (i) a buckling coefficient d_0 describing an exponential decrease in fiber stiffness under compression, (ii) linear stiffness κ_0, (iii) critical strain for the onset of strain stiffening λ_s and (iv) an exponential strain stiffening coefficient d_s (**Fig. 1d,e**).

$$w''(\lambda) = \kappa_0 \begin{cases} e^{\lambda/d_0} & \forall \lambda < 0 \\ 1 & \forall 0 < \lambda < \lambda_s \\ e^{(\lambda-\lambda_s)/d_s} & \forall \lambda_s < \lambda \end{cases} \quad (1)$$

With a mean field approach, the deformation λ of a fiber is defined by the change in length Δl relative to the fiber's end-to-end distance in the unstressed state, $\lambda = \Delta l/l$. The value of λ is determined by the fiber displacement field $\vec{U}$ and the local average deformation field $F = \text{grad }\vec{U}$ according to

$$\lambda = |F\vec{e}_\Omega| - 1 \quad (2)$$

with unit vector $\vec{e}_\Omega$ pointing in the direction of the fiber orientation Ω. The mechanical stress of the fiber is then

$$w'(\lambda) = \int_0^\lambda w''(\lambda)d\lambda$$

Integration from zero implies that the material has no pre-stress. One can derive a constitutive equation that relates the nominal stress tensor N to the deformation field F by averaging the stress contributions of many fibers, assuming an isotropic and homogeneous distribution[12] (**Supplementary Note 2**).

$$N_{ij} = \left\langle w'(|F\vec{e}_\Omega| - 1)\frac{(F\vec{e}_\Omega)_i \cdot (\vec{e}_\Omega)_j}{|F\vec{e}_\Omega|} \right\rangle_\Omega \quad (3)$$

Rheometer experiment. We used a cone-plate rheometer to measure the stress-strain relationship of collagen gels for simple shear deformation. The collagen was polymerized inside the rheometer setup. The cone-plate rheometer applied a simple shear deformation such that the strain energy density depended only on the engineering shear strain. We obtained the linear stiffness κ_0, the stiffening coefficient d_s and the characteristic strain λ_s at the onset of stiffening by minimizing the error between the measured and computed stress-strain relationships (**Supplementary Note 4**).

Uniaxial stretch experiment. We cast collagen gel, fibrin gel or Matrigel into a flexible polydimethylsiloxane dish with a sulfo-SANPAH (sulfosuccinimidyl 6-(4′-azido-2′-nitrophenylamino) hexanoate) activated surface. After polymerization, the gel in the dish was stretched uniaxially at a rate of 6% per hour with a stepper-motor device[33], and the height of the gel as a function of applied stretch was measured with a microscope[34]. We fit the buckling coefficient d_0 of our constitutive equation (equation (3)) to best match the measured relationship of vertical versus horizontal strain. We took the other three material parameters of the constitutive equation from the shear rheometer experiment (**Supplementary Note 4**) in the case of collagen and from extensional rheometer experiments in the cases of fibrin and Matrigel.

The vertical contraction of a gel under horizontal stretching can be converted to an apparent Poisson's ratio, which in the case of collagen is considerably greater than 1. According to linear elastic theory, a Poisson's ratio of >0.5 leads to a negative bulk modulus, implying that the undeformed configuration of the material is unstable. The Poisson's ratio of a hydrogel, however, is that of the composite material, which in the case of a collagen gel consists of collagen fibers and water. When a collagen gel is stretched, water can be released. Moreover, the apparent Poisson's ratio of a collagen gel is highly asymmetric and nonlinear. For compression, the apparent Poisson's ratio is much less than 0.5 (**Fig. 1b**).

Extensional rheometer. For measuring the stress-strain relationship under uniaxial stretch, a cylinder of collagen, fibrin or Matrigel was cast between two parallel plates (diameter, 5 cm; gap, 3 mm) (**Fig. 2a**). The lower plate was connected to a precision scale (AND GR-200), and the upper plate was mounted on a motorized micromanipulator (Eppendorf Injectman). The gel was extended at a rate of 10 µm/s, and the weight was continuously recorded. The force-extension curve of the gel was corrected for the mechanical compliance of the device. The stress-strain relationship was computed from the corrected force-extension curve and the known geometry of the gel cylinder. The material parameters were then obtained as described for the shear rheometer experiment (**Supplementary Note 4**).

Finite-element method. To solve the constitutive equation (equation (3)) for arbitrary geometries and boundary conditions, we used a finite-element method in which the material was represented by a mesh of mechanically coupled tetrahedra. Given a set of displacements of the nodes (cornerpoints of the tetrahedra), we calculated the nodal forces as the derivative of the total strain energy of the material by the displacements of the respective nodes (**Supplementary Note 2**). In the case of a point-like

force applied to the surface of a gel, the mesh also included the free top surface. All other boundaries were fixed. The considered gel region around a cell was larger than 480 µm.

Magnetic-tweezers experiment. We measured the material displacement field in response to a point-like force at the surface by applying a lateral force of 10–30 nN to a superparamagnetic bead (Microparticles Berlin, Germany; diameter, 5 µm) with magnetic tweezers[5,35]. The gel was decorated with 1-µm fluorescent beads (FluoSpheres, Molecular Probes) that served as fiducial markers. A stack of images around the magnetic bead was acquired before and 10 min after the onset of force application. The displacement of each fluorescent marker was then obtained from the image data as described in ref. 5. The measured displacements were interpolated to a regular finite-element mesh with a grid constant of 7.5 µm in the case of unconstrained force reconstruction, or to an irregular mesh with increasing mesh density near the magnetic bead in the case of constrained (point-like) force reconstruction. The coefficient of variation (CV) of the bead radius was ~5% as stated by the manufacturer, which led to an error (CV) of the applied force of 15%.

Constrained force reconstruction through direct fitting. Given a set of measured displacements of fluorescent markers inside a gel, we minimized the mismatch between the simulated and the measured gel displacements by shifting the location of force application in the simulation, as well as by adjusting the force amplitude and direction. The simulated displacement fields were calculated for a discrete set of force amplitudes and were linearly interpolated between these discrete solutions. The simulated displacement field was shifted, rotated and interpolated onto the positions of the fluorescent markers for which the displacement was measured. We then minimized the least-square error by randomly varying the shift, rotation and amplitude parameters until convergence was reached.

Cell culture. Cells were cultured in 25-cm^2 flasks without surface coating in DMEM (1 g/l D-glucose) with 10% FBS, 1% penicillin and streptomycin at 37 °C, 5% CO$_2$ and 95% humidity. Cells were passaged every 3 d. Trypsin-EDTA was used to detach cells. Cells were mixed with collagen solution before polymerization at a concentration of 15,000 cells/ml and incubated for 12 h before experiments. MDA-MB-231 breast carcinoma cells were obtained from ATTC; dual-color H2B-GFP/cytoplasmic TagRFP HT1080 fibrosarcoma cells were a gift from Katarina Wolf and were generated by Esther Wagena (Radboud University Nijmegen). All cell lines were checked with a mycoplasma PCR detection kit (Minerva Biolabs).

Fiber-pattern matching. To measure the displacement field of the matrix surrounding the cells, we imaged the collagen network directly using confocal reflection microscopy (Leica SP5X, 20× dip-in water-immersion objective (numerical aperture (NA) 1.0)). Confocal reflection microscopy needs only low laser intensities and prevents photodamage of the cells. From two stacks of confocal reflection images (voxel size of 0.72 µm in all dimensions, field of view of 370 µm in all dimensions) that were taken before and after cell force relaxation with cytochalasin D, we obtained the cell-induced deformation field over a regular grid with

a 7.5-µm mesh size by particle image velocimetry as follows. The algorithm we used calculated the cross-correlation between corresponding local sections (12 × 12 × 12 voxels) of the two stacks. It then shifted the section of the first stack by subvoxel increments using trilinear interpolation. This shift corresponded to a displacement vector. To find the local displacement with the highest cross-correlation, we used the downhill simplex method[36]. The accuracy of the deformation measurements was 60 nm (r.m.s.) (**Supplementary Note 12**). For 1.2-mg/ml gels with an average pore size of 3.8 µm, the optimal mesh size of the gel subvolumes used for cross-correlation, and thus the spatial resolution of the algorithm, was 7.5 µm (**Supplementary Note 12**).

Force reconstruction. We reconstructed the 3D force field (force per volume) inside a continuous material, assuming that cellular forces could exist everywhere inside the considered volume. This left us with a computational problem, as the number of fitted parameters (force vectors) equaled the number of data points (measured displacement vectors). We therefore used a regularization method. We performed regularization by minimizing a target function ($\underline{u}$) that was the sum of the ordinary least-square displacement error and a locally weighted norm of the nodal forces.

$$L(\underline{u}) = \left\| \underline{u} - \underline{u}_{\text{measured}} \right\|_{\underline{\underline{P}}}^2 + \left\| \underline{f(\underline{u})} \right\|_{\underline{\underline{A}}}^2$$

where $\left\| \underline{x} \right\|_{\underline{\underline{Q}}}^2$ denotes $\underline{x}^T \underline{\underline{Q}} \underline{x}$. The diagonal matrix $\underline{\underline{P}}$ has a value of 1 if the displacement of the corresponding node is known and a value of 0 if the displacement reconstruction algorithm is not able to measure the local displacement, or if the corresponding node lies outside of the imaged section. The matrix $\underline{\underline{A}}$ is a diagonal matrix containing the local penalty weights. If $\underline{\underline{A}}$ is proportional to the identity matrix (this corresponds to the Tikhonov regularization method), all nodal forces are penalized and therefore underestimated. To address this issue, we used the maximum-likelihood regression method, which iteratively assigns a lower penalty weight to nodes that have a high force[37].

$$A_{ii} = \begin{cases} \alpha, |f_i| < 1.345 \cdot median(|\underline{f}|) \\ \dfrac{\alpha \cdot 1.345 \cdot median(|\underline{f}|)}{|f_i|}, |f_i| > 1.345 \cdot median(|\underline{f}|) \end{cases}$$

This procedure reliably penalizes forces due to uncorrelated displacement noise but not cell forces, which are accompanied by long-ranging and correlated displacements. Thus, the algorithm finds the cell forces in an unconstrained manner. It is also possible to constrain the forces to the surface of the cell by predefining low or zero values for the local-penalty-weight matrix $\underline{\underline{A}}$ at specific points corresponding to the cell surface (**Supplementary Note 18**).

The locally weighted norm of the nodal forces, $\left\| \underline{f(\underline{u})} \right\|_{\underline{\underline{A}}}^2$, is nonlinear in $\underline{u}$, and therefore $L(\underline{u})$ cannot be easily minimized. We expanded $\underline{f(\underline{u})}$ as a first-order Taylor series for nodal displacements $\underline{u} + \underline{\Delta u}$ (**Supplementary Note 9**), using the stiffness tensor K (**Supplementary Note 3**).

$$L(\underline{u} + \underline{\Delta u}) = \left\| \underline{u} + \underline{\Delta u} - \underline{u}_{\text{measured}} \right\|_{\underline{\underline{P}}}^2 + \left\| \underline{f_u} + \underline{\underline{K_u}} \cdot \underline{\Delta u} \right\|_{\underline{\underline{A}}}^2$$

To find the value of $\underline{\Delta u}$ that minimized this expression, we solved the following equation using the conjugate gradient method[38]:

$$(\underline{\underline{P}} + \underline{K_u} \cdot \underline{\underline{A}} \cdot \underline{K_u}) \cdot \underline{\Delta u} = \underline{\underline{P}} \cdot (\underline{u_{\text{measured}}} - \underline{u}) - \underline{K_u} \cdot \underline{\underline{A}} \cdot \underline{f_u}$$

We then added $\underline{\Delta u}$ to the estimated nodal displacements $\underline{u}$ and updated the Taylor coefficients $\underline{f_u}$ and $\underline{K_u}$ and the local weight matrix $\underline{\underline{A}}$ for the next iteration until convergence was reached.

To compute the total contractility of a cell without bias caused by noise forces from regions outside the cell, we computed for every node $\vec{r_n}$ of the gel the contractile force C_{tot} as the scalar product of the force at that node with a unit vector pointing toward the cell force center $\vec{r_c}$ (ref. 39) (**Supplementary Note 13**).

The source code of the algorithm, including the 3D particle image velocimetry and the unconstrained force reconstruction, is available under MIT license on the collaborative coding platform GitHub (https://github.com/Tschaul/SAENO) and is free to download. A compiled version of the software and a tutorial are provided as **Supplementary Software**, together with a sample data set (http://lpmt.biomed.uni-erlangen.de/3DTractions/SampleData.rar).

Analysis of cell migration. We extracted the center-of-mass movement of the cells from their brightfield projections. The movement of the center of mass is described as a persistent random motion with time-varying migratory activity and migratory persistence. We extracted the time courses of both of these parameters from the measured trajectories using a Bayesian method of sequential inference[28]. Only cells that were not undergoing cell division during measurements were included in the correlation analysis.

Statistical analysis. Differences between measurements were considered statistically significant at $P < 0.05$ by Student's two-tailed t-test assuming unequal variances.

33. Bonakdar, N. *et al.* Biomechanical characterization of a desminopathy in primary human myoblasts. *Biochem. Biophys. Res. Commun.* **419**, 703–707 (2012).
34. Faust, U. *et al.* Cyclic stress at mHz frequencies aligns fibroblasts in direction of zero strain. *PLoS ONE* **6**, e28963 (2011).
35. Kollmannsberger, P. & Fabry, B. High-force magnetic tweezers with force feedback for biological applications. *Rev. Sci. Instrum.* **78**, 114301 (2007).
36. Nelder, J.A. & Mead, R. A simplex method for function minimization. *Comput. J.* **7**, 308–313 (1965).
37. Huber, P.J. *Robust Statistics* (John Wiley & Sons, 1981).
38. Tikhonov, A.N. Solution of incorrectly formulated problems and the regularization method. *Soviet Mathematics Doklady* **4**, 1035–1038 (1963).
39. Hersch, N. *et al.* The constant beat: cardiomyocytes adapt their forces by equal contraction upon environmental stiffening. *Biol. Open* **2**, 351–361 (2013).